nature energy

Article

https://doi.org/10.1038/s41560-023-01317-5

Efficient hole abstraction for highly selective oxidative coupling of methane by Au-sputtered TiO_2 photocatalysts

Received: 26 March 2023

Accepted: 29 June 2023

Published online: 17 August 2023

Check for updates

Xiyi Li[1], Chao Li[2], Youxun Xu[1], Qiong Liu[3], Mounib Bahri[4], Liquan Zhang[5], Nigel D. Browning[4], Alexander J. Cowan[2] ✉ & Junwang Tang[1,6] ✉

Photocatalytic oxidative coupling of methane (OCM) produces C_2 molecules that can be used as building blocks for synthesis of fuels and chemicals. However, the yield rate and the selectivity of C_2 products are still moderate due to the stable nature of methane molecules. Here we develop a Au nanocluster-loaded TiO_2 photocatalyst by a sputtering approach, achieving a high methane conversion rate of 1.1 mmol h^{-1}, C_2 selectivity of ~90% and apparent quantum efficiency of 10.3 ± 0.6%. The high C_2/C_{2+} yield rate is on the same order of magnitude as the benchmark thermal catalysts in OCM processes operated at high temperature (>680 °C). Au nanoparticles are shown to prolong TiO_2 photoelectron lifetimes by a factor of 66 for O_2 reduction, together with Au acting as a hole acceptor and catalytic centre to promote methane adsorption, C–H activation and C–C coupling. This work underscores the importance of multifunctional co-catalysts and mechanistic understanding to improve photocatalytic OCM.

The abundant reserves of methane have triggered a tremendous number of studies on the direct conversion of methane to value-added fuels and chemicals[1]. Oxidative coupling of methane (OCM) to C_2 (C_2H_6 and C_2H_4) products is regarded as one of the most important catalytic technologies in industry and academia[2,3]. However, the inert nature of methane, for example, the high C–H bond energy (439 kJ mol^{-1}), means that harsh reaction conditions are required to convert it[4]. Thus none of the thermocatalysts reported so far is economically viable due to the high reaction temperature, coking, catalyst sintering and/or irreversible overoxidation[4–7].

Photocatalytic methane conversion provides an attractive alternative, including both photocatalytic non-oxidative coupling of methane and photocatalytic OCM. The former converts methane to form valuable products, ethane and hydrogen, achieving 100% atom utilization efficiency. However, due to the thermodynamically unfavourable nature of this process ($\Delta G° = 68.6$ kJ mol^{-1}), the yield rate is always very low despite the involvement of energetic charge carriers excited by photons[1]. In most cases, coke accumulation could happen as a thermodynamically more favourable process ($\Delta G° = 50.7$ kJ mol^{-1}) under anaerobic conditions[8]. In contrast, photocatalytic OCM is a thermodynamically feasible reaction with the assistance of oxygen; thus, the product yield is always rather high, but overoxidation to CO_2 is very hard to avoid owing to the inevitable existence of superoxide radicals.

Various photocatalysts have shown great potential in methane coupling to C_2 products with high selectivity (from 60% to ~99%), such as Pt-CuO_x/TiO_2 (ref. 9), Pd–Bi/Ga_2O_3 (ref. 10), Au–ZnO/TiO_2 (ref. 11) and $Zn_5(OH)_8Cl_2{\cdot}H_2O$ (ref. 12). However, all the methane coupling photocatalysts exhibit only a moderate methane conversion rate at the level of μmol h^{-1}, and some of them were even less than 1 μmol h^{-1}, resulting in a C_2 yield rate ~10–1,000 times lower than those

[1]Department of Chemical Engineering, University College London, London, UK. [2]Stephenson Institute for Renewable Energy, University of Liverpool, Liverpool, UK. [3]Institute of Analysis, Guangdong Academy of Sciences (China National Analytical Center, Guangzhou), Guangzhou, China. [4]Albert Crewe Centre for Electron Microscopy, University of Liverpool, Liverpool, UK. [5]Department of Chemistry, University College London, London, UK. [6]Industrial Catalysis Center, Department of Chemical Engineering, Tsinghua University, Beijing, China. ✉e-mail: acowan@liverpool.ac.uk; junwang.tang@ucl.ac.uk

reported by thermocatalysis. The fabrication procedures of these photocatalysts are time consuming, making them less attractive for practical application.

Three fundamental factors are crucial for an efficient photocatalyst, including light harvesting, charge separation and surface reactions of charges[1]. The selection of a co-catalyst often plays a key role in promotion of charge separation and control of surface reactivity. Gold as a widely used co-catalyst has various functions, such as enhancing light absorption[13], facilitating charge transfer[14], and control selectivity[15]. It is interesting to read that the role of Au is often proposed as an electron acceptor to accelerate O_2 reduction[11]. However, CH_4 activation by photoholes is more challenging and important than O_2 reduction in OCM processes as the former dominates the yield and selectivity of the final products.

In this Article, a rapid sputtering method has been developed to homogeneously load Au co-catalyst on TiO_2. The optimized sample Au60s/TiO_2 after only 60 s sputtering presents a methane conversion rate of approximately 1.1 mmol h^{-1}, a selectivity at around 90% and a high apparent quantum efficiency (AQE) of 10.3 ± 0.6% at 365 nm. The multi-roles of Au are revealed as a photohole acceptor, adsorption site and selective activation centre.

Photocatalytic OCM activity

A rapid sputtering method was developed to efficiently prepare a supported Au/TiO_2 photocatalyst on a glass fibre membrane (Supplementary Figs. 1 and 2 and Supplementary Notes 1 and 2). The ultraviolet–visible (UV–Vis) absorption properties of the as-prepared membranes were investigated as shown in Supplementary Fig. 3 and Supplementary Note 3.

The photocatalytic OCM activity of these Au/TiO_2 membranes was then evaluated in the flow reactor (Supplementary Fig. 4). The optimum sputtering time of Au was first investigated on 5 mg TiO_2 (Fig. 1a,b). The main product over pure TiO_2 is CO_2, while the major product for Au/TiO_2 is C_2H_6, together with CO_2 and C_3H_8 and trace amounts of other hydrocarbon products. The selectivity is significantly shifted to C_2 products once Au is introduced, from 4% over pure TiO_2 to more than 75% over all Au/TiO_2 catalysts. The C_2 yield rate exhibits a volcano trend with the increasing Au sputtering time, reaching the highest value (176 μmol h^{-1}) with an excellent selectivity of 87% at 60 s sputtering time (Au60s/TiO_2 sample). This is the highest C_2 yield rate among all the reported photocatalytic methane conversion processes (Supplementary Table 1). The 60 s sputtering time also gives a CH_4 conversion rate as high as 404 μmol h^{-1}, 2.3 times higher than that of pristine TiO_2, suggesting a higher utilization efficiency of photo-induced charges and more effective methane activation. Further increasing the amount of Au can slightly increase the C_2 selectivity, while the C_2 yield rate decreases to a larger extent. As discussed in the UV–Vis absorption spectra, an excessive amount of Au nanoparticles can lead to a strong scattering effect, which is detrimental to the effective light absorption.

The amount of TiO_2 was also investigated (Supplementary Fig. 5). The C_2 yield rate increases with the higher amount of TiO_2, reaching 287 μmol h^{-1} with 20 mg TiO_2, while the C_2 selectivity remains similar at around 88%. However, when the amount of TiO_2 exceeds 20 mg, the yield rate of C_2 products can hardly increase. This is because the light cannot penetrate the thicker TiO_2 layer, which will be discussed later. Thus, the optimum amount of TiO_2 is 20 mg, while the ideal Au sputter time is 60 s and the mass of Au is estimated to be 0.38 mg based on the calibration curve in Supplementary Fig. 2.

This optimum photocatalyst membrane was then used for the further investigation of different reaction parameters. The influence of different reaction temperatures was studied (Supplementary Fig. 6). The C_2 yield rate can be further increased by raising the reaction temperature, from 287 μmol h^{-1} at 338 K to 388 μmol h^{-1} at 393 K. However, further increasing the temperature to 413 K cannot contribute to an increase in the yield rate, probably due to the decreased adsorption of reactants on the catalyst surface or the enhanced recombination of charge carriers[16,17]. The C_2 selectivity remains almost constant at 90% at different temperatures, indicating the stable performance of Au even under relatively high temperatures.

The concentration of O_2 would play an important role in OCM, thus different flow rates of air were investigated (Fig. 1c). Expectedly, both the conversion rate of CH_4 and the selectivity of C_2 products increase with more available O_2 molecules. When the flow rate of air reaches 12 ml min^{-1}, the CH_4 conversion rate and the yield rate of C_2 products can reach as high as 1.09 mmol h^{-1} and 468 μmol h^{-1}, resulting in a C_2 selectivity of 86%. This is because a higher concentration of O_2 can promote the generation of superoxide radicals, benefiting the conversion of methane while also promoting the overoxidation to CO_2 (ref. 9). Therefore, it is reasonable to see an increase of CO_2 production when an air flow rate of 15 ml min^{-1} was applied, which is nearly 10% increase compared with that at the flow rate of 12 ml min^{-1}. Considering a small increase of only 1.4% in the C_2 yield rate but a 10% increase in the CO_2 production at the flow rate of 15 ml min^{-1}, 12 ml min^{-1} was selected as the optimum air flow rate for subsequent investigation. The optimized experimental condition is the gas hourly space velocity (GHSV) of 977,430 ml g_{cat}^{-1} h^{-1} operated at 393 K. The C_2 yield rate under this optimized condition is 133 times higher than pristine TiO_2.

The stability of Au60s/TiO_2 was also evaluated under this optimized reaction condition (Fig. 1d and Supplementary Fig. 7). Au60s/TiO_2 shows a stable C_2 yield rate and C_2H_4/C_2H_6 ratio in a 30 h run despite of the fluctuation of the gas flow, unlike the thermal catalysts that often suffer from the deactivation of sintering or coke accumulation at high temperature. Furthermore, the chemical state of Au remains almost unchanged after the stability test, as discussed later in the characterization section. The high stability of Au60s/TiO_2 may benefit from the relatively mild photocatalytic reaction condition. Finally, a series of control experiments with $^{13}CH_4$ isotope labelling experiment were then carried out to confirm the carbon source of the products (Supplementary Fig. 8 and Supplementary Note 4).

To gain a reliable and reproducible activity of this photocatalyst, four Au/60s TiO_2 (20 mg TiO_2) on glass fibre membranes were fabricated at different batches and tested under the optimized conditions (Supplementary Fig. 9). The C_2 yield rate and C_2 selectivity are similar over four different samples, indicating the high reproducibility of this preparation method and activity. The average methane conversion rate over the optimized sample Au60s/TiO_2 under the optimized condition is 1.12 ± 0.04 mmol h^{-1} with a high selectivity of about 90% to desired products (86% to C_2 and 93% to C_{2+}). The corresponding AQE of these four membranes was also obtained (Supplementary Fig. 10) and the Au60s/TiO_2 membrane on average exhibits a high AQE of 10.3 ± 0.6 at 365 nm. As shown in Fig. 1e and Supplementary Table 1, to the best of our knowledge such high methane conversion rate and AQE are the highest so far achieved for photocatalytic OCM.

Such excellent activity of Au60s/TiO_2 allows the comparison with those representative OCM catalysts by thermocatalysis (Supplementary Fig. 11 and Supplementary Table 2). The yield rate of C_2/C_{2+} products over Au60s/TiO_2 is comparable to those classic thermal catalysts operated at a significantly higher temperature (at least 560 K higher). Interestingly, Au60s/TiO_2 exhibits at least ~20% higher C_2/C_{2+} selectivity (ca. 90%) to those benchmark thermocatalysts. This can greatly improve the carbon atom utilization efficiency of methane and avoid the massive production of CO_2/CO in thermocatalysis, consistent with the low carbon perspective.

Structural characterization

The structure of the as-prepared Au/TiO_2 membranes was then investigated and the optimized sample Au60s/TiO_2 was fully characterized to correlate the performance with the catalyst structure. The X-ray diffraction (XRD) patterns were used to examine the crystal structure (Supplementary Fig. 12). All XRD patterns show the typical peaks assigned to the anatase TiO_2 (JCPDS no. 84-1286). No peaks for Au

https://doi.org/10.1038/s41560-023-01317-5

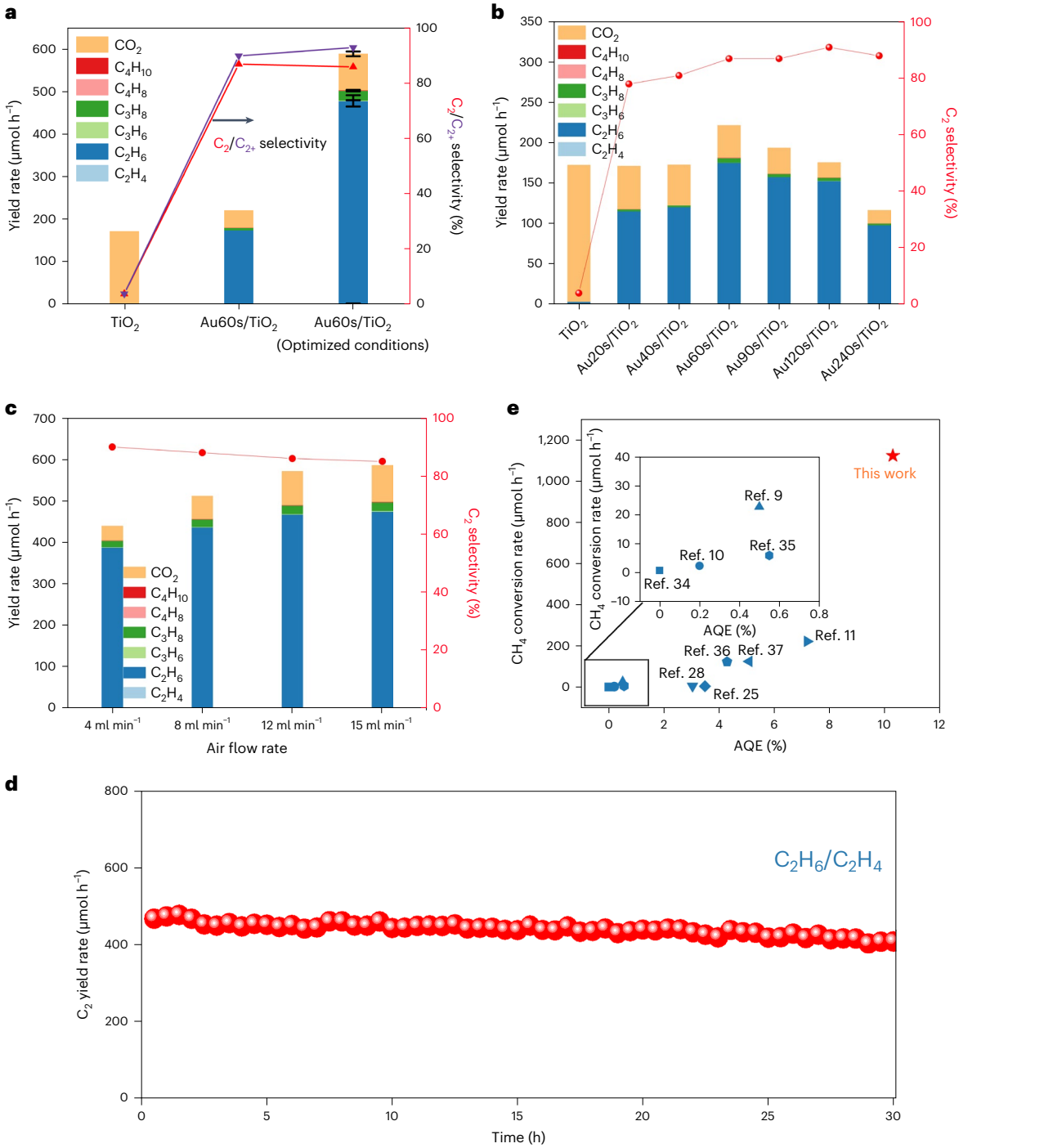

Fig. 1 | Photocatalytic OCM on Au/TiO_2. **a**, The photocatalytic OCM activity over TiO_2 and Au60s/TiO_2 (reaction condition: 320 ml min^{-1} CH_4 and 4 ml min^{-1} air, 365 nm LED 100 W, 5 mg catalyst, 338 K) and the photocatalytic OCM activity over Au60s/TiO_2 under optimized conditions (reaction condition: 320 ml min^{-1} CH_4, 12 ml min^{-1} air, 393 K, 365 nm LED 100 W, 20 mg catalyst). Note: the error bar (standard deviation) of activity over Au60s/TiO_2 at optimum conditions was obtained by four samples from different batches. The average used is the mean value. The data of the third column (Au60s/TiO_2 under optimum conditions) are presented as the mean values ± standard error of the mean. **b**, Photocatalytic OCM activity over Au/TiO_2 with different Au sputtering times (Au 0 s, Au 20 s, Au 40 s, Au 60 s, Au 90 s, Au 120 s, Au 240 s) on 5 mg TiO_2 (reaction condition: 320 ml min^{-1} CH_4 and 4 ml min^{-1} air, 365 nm LED 100 W, 338 K). **c**, Photocatalytic OCM activity over Au60s/TiO_2 at 393 K with different air flow rates (reaction condition: 20 mg TiO_2, 320 ml min^{-1} CH_4, 365 nm LED 100 W). **d**, Stability test of Au60s/TiO_2 under the optimized reaction condition (reaction condition: 20 mg TiO_2, 320 ml min^{-1} CH_4, 12 ml min^{-1} air, 393 K, 365 nm LED 100 W). **e**, Summary of OCM rate and AQE ($\lambda < 400$ nm) achieved in this work and other representative studies (Pt/Ga–TiO_2–SiO_2 (ref. 34), Pd–Bi/Ga_2O_3 (ref. 10), Pt–CuO_x/TiO_2 (ref. 9), (Zn^+, Zn_2^+)–ZSM-5 (ref. 35), Pd_1/TiO_2 (ref. 28), Ag–$H_3PW_{12}O_{40}$/TiO_2 (ref. 25), Au/Ga_2O_3 (ref. 36), Pd/Ga_2O_3 (ref. 37), Au–ZnO/TiO_2 (ref. 11)). The detailed reaction condition and other 14 photocatalysts without the reported AQE are presented in Supplementary Table 1. The inset graph is the zoomed rectangle area including four photocatalysts.

species are observed even after the 90 s sputter process (ca. 2.9 wt.%), probably owing to the high dispersion of Au as small nanoparticles, which is confirmed by scanning transmission electron microscopy (STEM) later.

The morphology of the Au60s/TiO_2 glass fibre membrane was investigated by scanning electron microscopy (SEM) (Fig. 2a–f). From the top view of the SEM image (Fig. 2a,b), the TiO_2 nanoparticles disperse homogeneously on the top of glass fibre membranes. While few

https://doi.org/10.1038/s41560-023-01317-5

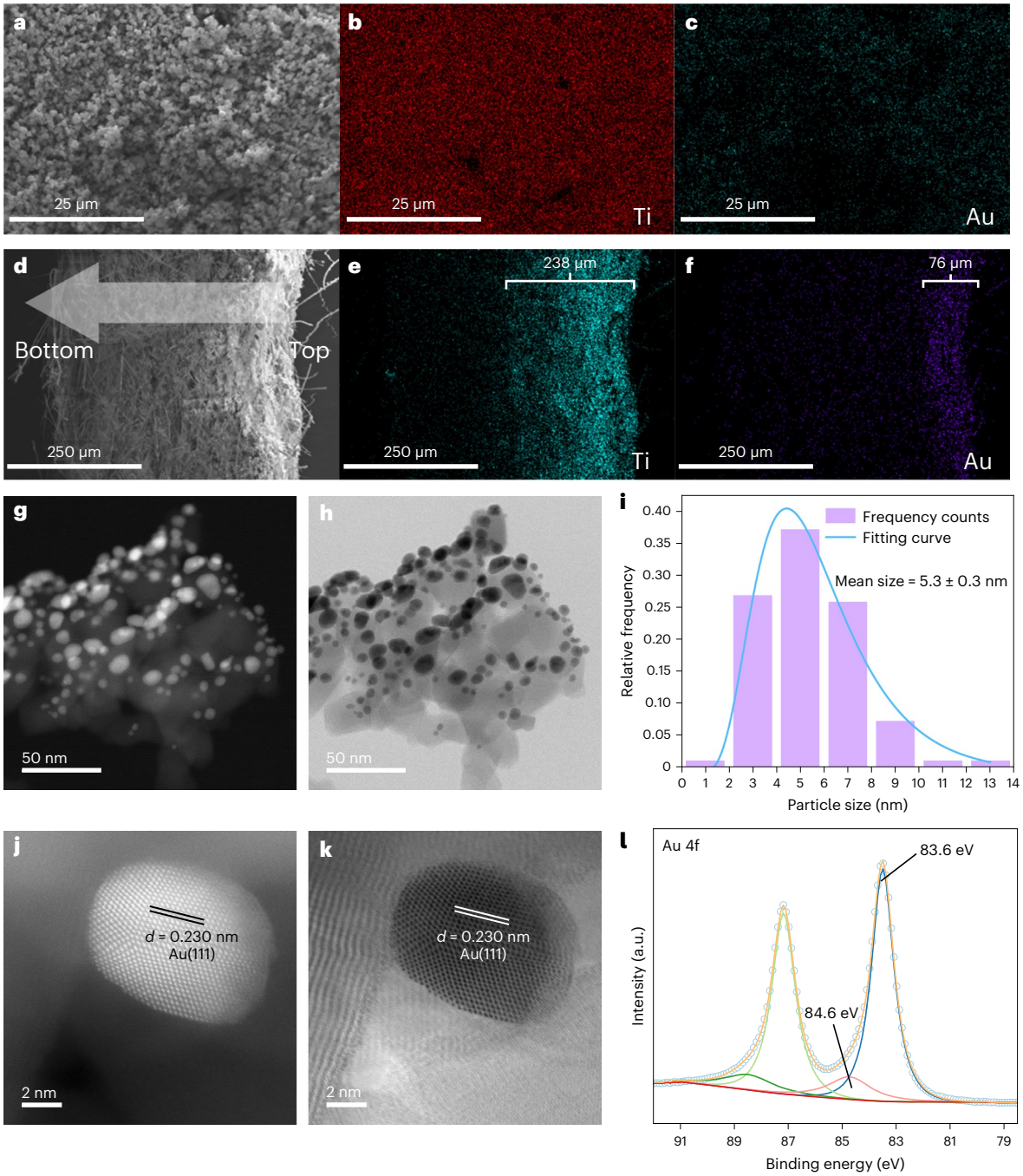

Fig. 2 | Structure characterization and analysis of Au60s/TiO_2. **a**–**c**, Top view SEM image (**a**) and EDX image of Au60s/TiO_2 membrane (**b** for Ti element, **c** for Au element). **d**–**i**, Side view SEM image (**d**) and EDX image of Au60s/TiO_2 membrane (**e** for Ti element, **f** for Au element). STEM-HAADF image of Au60s/TiO_2 (**g**), STEM-BF image of Au60s/TiO_2 (**h**), particle sizes distribution of Au on TiO_2. Note: 97 particles were counted. The fitting curve (**i**) was generated by log-normal model based on the bin centre and the relative frequency in origin. **j**,**k**, High-resolution STEM-HAADF image of Au nanoparticle (**j**) and high-resolution STEM-BF image of Au nanoparticle (**k**). **l**, The XPS spectra of Au 4f in Au60s/TiO_2. Note: the fitting curve of the Au 4f spectra employed Gaussian (10%)–Lorentzian (90%) peak shapes (defined as GL(90)) in CasaXPS software.

long glass fibres can extend to the TiO_2 layer from the side view of the SEM image (Fig. 2d), and the TiO_2 layer is approximately 238 μm on top of the fibre membrane (Fig. 2e). Using energy-dispersive X-ray (EDX) mapping, the distribution of Au on TiO_2 can be observed (Fig. 2c,f). The intensity of Au element decreases with the increasing depth of the membrane (Fig. 2f). This suggests that Au mainly locates on the top surface of the TiO_2 layer with a depth of about 76 μm, which is close to the light irradiation to drive methane conversion reaction. To gain more structure information on Au over Au60s/TiO_2 membrane, the sample was scratched from the membrane and used for STEM analysis (Fig. 2g–k). The STEM images show the distribution of small Au nanoparticles on the support of TiO_2, in which the Au nanoparticles are the bright spots in the high-angle annular dark-field image (STEM-HAADF, Fig. 2g) and the dark spots in the bright-field image (STEM-BF, Fig. 2h). The average particle size of the Au nanoparticles is determined to be 5.3 nm (Fig. 2i). These nanoparticles were further identified by high-resolution STEM images (Fig. 2j,k), where the *d* spacing of lattice fringes is 0.230 nm, corresponding to the Au(111) planes[13].

https://doi.org/10.1038/s41560-023-01317-5

The chemical state of Au in the Au60s/TiO_2 membrane was investigated by X-ray photoelectron spectroscopy (XPS) (Fig. 2l). Two types of Au species can be observed in the Au 4f spectra, in which the Au $4f_{7/2}$ at ca. 83.6 eV dominates the chemical states with a small number of species at around 84.6 eV. The difference in binding energy is 1.0 eV, smaller than that between Au(0) and Au(I) (ca. 2 eV) (ref. 18), and the major species is probably metallic Au (ref. 19). The Au 4f spectrum after a 30 h reaction remains similar to that before the reaction (Supplementary Fig. 13), suggesting the high stability of this photocatalyst. The Au $4f_{7/2}$ at ca. 83.6 eV still dominates the chemical state. The species peaking at ca. 84.6 eV before the reaction shift to the higher binding energy by ca. 1.2 eV after the reaction, probably owing to the hole acceptor nature of Au as shown later.

Investigation of photocatalytic mechanism

The influence of the catalyst mass on the light harvesting of the membrane was investigated by a double layer structure (TiO_2/$BiVO_4$) (Supplementary Fig. 14, discussion is shown in Supplementary Note 5), which explains that almost no yield rate increases when more TiO_2 (>20 mg) is loaded (Supplementary Fig. 5).

The contribution of Au itself via inter-band electronic transitions or surface plasma to drive the photocatalytic reaction is also discussed (Supplementary Figs. 15 and 16 and Supplementary Note 6), which indicates that TiO_2 rather than Au is the main light-harvesting material in this reaction.

Two types of photo-induced carriers (electrons and holes) are generated during the excitation of TiO_2. Transient absorption spectroscopy (TAS) is a sensitive technique to investigate the charge carrier dynamics, and it can be used to distinguish which carrier is transferred to Au and to experimentally identify the function of Au (the procedure to prepare Au/TiO_2 and TiO_2 glass slides for TAS observation is shown in Methods). The Au/TiO_2 glass slide shows similar activity to Au60s/TiO_2 particles, and we thus use it to run the TAS measurement to increase the signal-to-noise ratio (Supplementary Fig. 17).

Oxygen and methanol were used to identify the nature of excited states in TiO_2 (Supplementary Figs. 18–20). As expected, photo-induced absorption from 500 to 700 nm can be assigned to photoholes, while the photo-induced absorption at >850 nm is attributed to TiO_2 photoelectrons, similar to previous observations[20]. The assignments are discussed in Supplementary Note 7.

The TAS spectra of Au/TiO_2 on ultrafast (fs–ns) and slow (μs–s) timescales were acquired and compared with pristine TiO_2 (Fig. 3a,b and Supplementary Figs. 21–29). The ultrafast spectra of Au/TiO_2 are dominated by a bleaching of the Au Surface Plasmon Resonance (SPR) (~550 nm) and the presence of a new strong photo-induced absorption at 620 nm, which is assignable to the Au nanoparticle (Supplementary Fig. 21a–c). Although the Au SPR dominates the visible TAS on the picosecond timescale, complicating analysis of photohole kinetics (see below), we find it has minimal contribution at times >50 ps at wavelengths (>850 nm) where the TiO_2 photoelectron absorbs (Supplementary Fig. 21).

The ultrafast TAS kinetics at 900 nm shows that the addition of Au leads to a very slight increase in TiO_2 photoelectron lifetime on the ps–ns timescale (Supplementary Fig. 22). The lifetime of photoelectrons was investigated on slower timescales (Fig. 3a,b). The TiO_2 photoelectron lifetime increases by 66 times due to Au loading ($t_{50\%}$, defined as the time taken for 50% decrease in the amplitude of photo-induced absorption at 10 μs, TiO_2 = 45 μs, Au/TiO_2 = 3 ms.). This result suggests either that Au is a hole acceptor in the composite which retards the recombination of photoelectrons and photoholes, leading to a longer lifetime of photoelectrons, or that the Au nanoparticles form a junction with the TiO_2 providing a local field stabilization of the photogenerated carriers. We observe on slow timescales (10 μs to 1 ms) that a new bleach appears centred at 600 nm (Supplementary Figs. 23–25) for Au/TiO_2 samples but not for unmodified TiO_2. Spectroelectrochemical

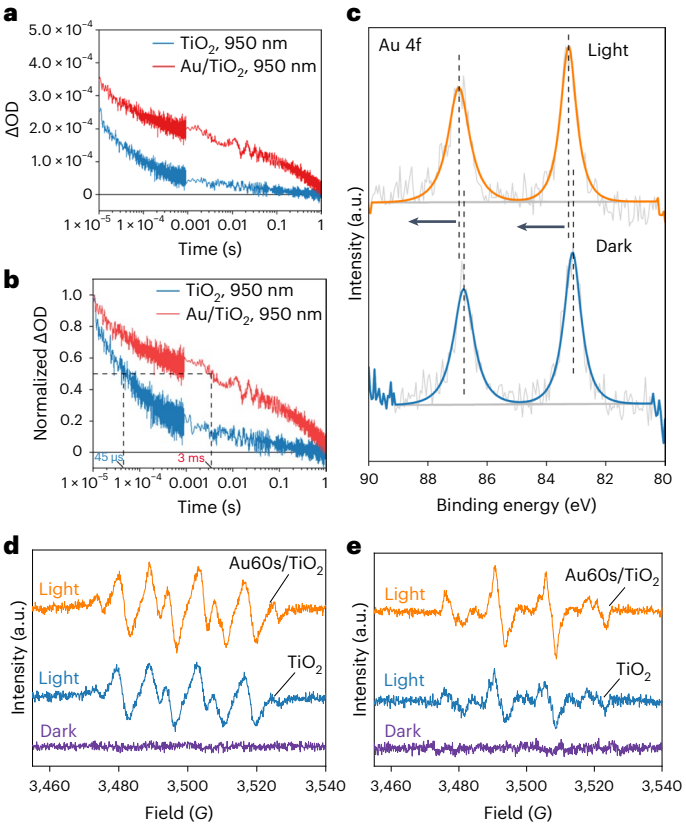

Fig. 3 | The investigation of charge dynamics and redox potential. a, TAS decay kinetics of TiO_2 and Au/TiO_2 probed at 950 nm excited by pump 355 nm under argon atmosphere. **b**, Normalization of TAS decay kinetics of TiO_2 and Au/TiO_2 probed at 950 nm and excited by pump 355 nm under argon atmosphere. Note: ΔOD refers to optical density change caused by the excitation. The dashed line in **b** indicates the corresponding timescale when the amplitude of ΔOD decreases by 50%. **c**, In situ XPS spectra of Au60s/TiO_2 (Au 4f) under dark and light irradiation conditions. Note: The fitting curve of the Au 4f spectra employed Gaussian (10%)–Lorentzian (90%) peak shapes (defined as GL(90)) in CasaXPS software. **d**, In situ EPR spectra of superoxide radicals using DMPO as a spin trap over TiO_2 and Au60s/TiO_2 in the CH_3OH aqueous solution under 5 min light irradiation using the EPR spectra of the solution mixture under dark condition as a reference. **e**, In situ EPR spectra of hydroxyl radicals using DMPO as a spin trap over TiO_2 and Au60s/TiO_2 in an aqueous solution under 5 min light irradiation using the EPR spectra of the solution mixture under dark condition as a reference.

measurements have shown that the application of a positive potential to indium tin oxide supported Au and Ag nanoparticles leads to a decrease in the plasmon absorbance, alongside a small frequency shift[21,22]. The observation of the bleaching of the Au plasmon mode on the microsecond timescale provides the support for hole transfer from the TiO_2 to Au. To confirm the kinetics of the proposed hole transfer only occurs on this slow timescale, it is desirable to directly monitor the TiO_2 hole lifetime. However, it was not possible for us to do so at present as the photohole absorption is spectrally overlapped with the oscillating optical response of the Au particles on the earlier (ps to ns) timescales[23].

To verify that the Au acts as a hole acceptor and to assess its potential role in O_2 reduction, the slow timescale transient absorption spectra (Supplementary Fig. 26) and the electron dynamics (Supplementary Fig. 27) were monitored when O_2 was introduced. On TiO_2, in the absence of Au, the electron-hole recombination is sufficiently fast that the $t_{50\%}$ of the photoelectron is indistinguishable in the presence and absence of O_2, indicating that minimal O_2 reduction occurs on TiO_2 alone (Supplementary Fig. 27a). Hole transfer to Au on Au/TiO_2 prolongs the photoelectron lifetime sufficiently, which reacts with

O_2 effectively ($t_{50\%}$ = 1.6 ms (Ar), $t_{50\%}$ = 230 µs (O_2) in Supplementary Fig. 27b). Methanol acts as a photohole scavenger on the ultrafast (ps) timescale. By preventing the charge recombination using methanol, we can compare the TiO_2 electron lifetimes to identify the timescale of O_2 reduction on both TiO_2 and Au/TiO_2 (Supplementary Fig. 27c,d). This experiment shows that O_2 reduction happens at the same rate on both materials, indicating that the site of O_2 reduction (the site of photoelectrons) is likely to be the TiO_2 and Au nanoparticles do not have a noticeable influence on the photoelectron reduction rate.

TAS experiments were also carried out to investigate the excitation of the plasmon band (λ_{ex} = 532 nm) of Au/TiO_2 (Supplementary Figs. 28 and 29 and Supplementary Note 8), which explains the observation of no activity by surface plasma-driven photocatalytic process (Supplementary Fig. 16b). In situ XPS was further conducted to investigate the charge transfer of Au60s/TiO_2 under the light irradiation (Fig. 3c). In the Au 4f spectra, a positive shift of 0.2 eV is observed when the sample is exposed to light, further suggesting that Au works as the hole acceptor. The band alignment between TiO_2 and Au is discussed in Supplementary Note 9. The transfer of photoholes from TiO_2 to Au can effectively decrease the oxidative potential of the original photoholes in TiO_2, thus avoiding the non-selective overoxidation to CO_2.

In the photocatalytic OCM process, two main half reactions will happen after the migration of photo-induced charges to the surface. One is the reduction of O_2 to form superoxide radicals by photoelectrons, and the other one is the oxidation of methane to form methyl radicals by photoholes, respectively. Therefore, in situ electron paramagnetic resonance (EPR) with 5,5-dimethyl-1-pyrroline-N-oxide (DMPO) as the spin trap reagent was conducted to monitor the generation of superoxide radicals over TiO_2 and Au60s/TiO_2 under light irradiation (Fig. 3d). Notably, a higher intensity of DMPO adduct is observed over Au60s/TiO_2 under light irradiation, suggesting a larger amount of superoxide radicals. As photoholes are extracted by Au, more photoelectrons with sufficient lifetime are left in TiO_2, which reduces oxygen to form more superoxide radicals and could promote the photocatalytic methane conversion cycle.

For the other half oxidation reaction by photoholes, it is necessary to evaluate the oxidation ability of photoholes after transferring to the d bands of the Au co-catalyst. The accurate work function of small Au species on Au60s/TiO_2 cannot be determined. Thus, there is a question that the photoholes potential on Au species may be too small for methane oxidation. The direct capture and observation of the methyl radicals are difficult and often interfered by other radicals. Hydroxyl radical with a more positive redox potential ($E^0(\cdot OH/H_2O)$ = 2.69 V, standard hydrogen electrode) than methane oxidation ($E^0(\cdot CH_3/CH_4)$ = 1.73 V, standard hydrogen electrode) was chosen for this study[24,25]. Au60s/TiO_2 exhibits a higher intensity of DMPO-OH adduct than that of pristine TiO_2 under light irradiation (Fig. 3e), suggesting that more hydroxyl radicals can be formed over Au60s/TiO_2. This confirms that the photoholes on Au are still able to activate the C–H bond in CH_4. Therefore, the introduction of Au can increase the amount of active photoholes to generate more products.

The in situ attenuated total reflectance–Fourier transform infra-red spectroscopy (ATR–FTIR) was used to investigate the adsorption of the reactant methane under dark condition and photocatalytic transformation of methane under light irradiation condition on TiO_2 and Au60s/TiO_2 (Fig. 4a–d and Supplementary Figs. 30–32). The typical C–H deformation vibration mode of CH_4 at ~1,306 cm^{-1} is observed after the introduction of CH_4 on both catalysts under dark condition (Fig. 4a,b)[26]. The intensity of this vibrational mode enhances significantly over Au60s/TiO_2, approximately nine times higher than that of pristine TiO_2 after 30 min of adsorption. In addition, a new noticeable peak at ~1,540 cm^{-1} gradually emerges on Au60s/TiO_2 with increasing the adsorption time, which is assigned to the C–H symmetric deformation vibrational mode or bending mode of methane[27]. No similar peak can be observed over pristine TiO_2. This suggests that the introduction of Au can effectively enhance methane adsorption, which is also one key step for the methane conversion.

To investigate other functions of Au during the photocatalytic process, in situ ATR–FTIR was then carried out with light irradiation (Fig. 4c,d and Supplementary Figs. 31 and 32). Upon light irradiation, the band assigned to the C–H vibration mode of CH_4 at ~1,306 cm^{-1} exhibits a decreasing trend with increasing time over both catalysts. Notably, this band on Au60s/TiO_2 shows nine times higher intensity than that on pristine TiO_2 at time 0 min, while decreases to a similar intensity on both catalysts after 10 min illumination (Supplementary Fig. 31). This result suggests the existence of Au nanoparticles can facilitate the methane conversion.

Moreover, the CH_2/CH_3 deformation vibrational modes at around 1,436 and 1,420 cm^{-1} (the selected region of Fig. 4c,d as shown in Supplementary Fig. 32a,b) only appears and enhances on Au60s/TiO_2 under light irradiation, indicating the rapid dissociation of CH_4 to CH_x (x = 3, 2) on the surface of Au60s/TiO_2 (ref. 28). Meanwhile, the peak at ca. 876 cm^{-1} (zoom-in in Supplementary Fig. 32d) corresponding to the C–C stretching[29], also enhances gradually with longer light illumination time, further demonstrating the efficient C–H abstraction of methane and C–C coupling formation to ethane. In contrast, another broad infra-red (IR) band (900 to 1,200 cm^{-1}, zoom-in in Supplementary Fig. 32c) that is attributed to either the bridging or terminal C–O stretching vibration mode at ~956 cm^{-1} and ~1,042 cm^{-1} keeps rising on pristine TiO_2 apart from the C–C stretching at ~876 cm^{-1} (refs. 27,29); the former is probably related to the process of CO_2 formation (the detailed analysis is shown in Supplementary Note 10)[30].

More importantly, another IR band at 690–740 cm^{-1} (zoom-in in Supplementary Fig. 32f) assigned to CH_3 rock in Au–CH_3 can only be detected over Au60s/TiO_2 (ref. 31), providing further evidence that CH_4 can be activated on Au nanoparticles. Previous density functional theory calculations also indicated that positively charging of Au nanoparticle (for example, charge transfer to TiO_2) could selectively enhance the CH_4 adsorption by bonding[32], consistent with the observation in our experiment. Thus, the selective C–H bond cleavage process and the C–C coupling process happen on the Au nanoparticles, effectively avoiding the direct oxidation of photoholes in TiO_2.

The function of Au on the reaction kinetics of the photocatalytic OCM was also investigated (Fig. 4e, Supplementary Fig. 33 and Supplementary Note 11). The incorporation of Au reduces the activation energy (E_a) from 7.7 kJ mol^{-1} over pure TiO_2 to ca. 5.5 kJ mol^{-1} over Au60s/TiO_2 (Fig. 4e), highlighting the extra function of Au during the activation of CH_4. Such low E_a enables the comparable selectivity and activity of Au60s/TiO_2 at room temperature to that attained by conventional high-temperature thermal catalysis (Supplementary Fig. 11 and Supplementary Table 2). The universality of Au's function was further confirmed by using ZnO instead of TiO_2 as the substrate (Supplementary Fig. 34 and Supplementary Note 12).

The mechanism of photocatalytic OCM reaction over Au/TiO_2 membrane is then proposed in Fig. 4f. Upon 365 nm light irradiation, electrons are excited from the valence band of TiO_2 to its conduction band, while the photoholes are transferred to the Au nanoparticles, generating long-lived photoelectrons on TiO_2 for oxygen reduction. Au can preferably adsorb CH_4, then photoholes on Au can effectively and selectively break the C–H bond of the pre-adsorbed CH_4 molecules to generate methyl radicals and protons. The combination of methyl radicals gives ethane molecules while the protons can be removed by superoxide radicals to form water. After the formation of ethane, these molecules can follow similar coupling mechanisms, for example, coupling methane to generate longer-chain hydrocarbons or to form olefin via the side dehydrogenation processes (detailed discussion in Supplementary Note 13)[33].

Conclusions

In summary, efficient photocatalyst Au60s/TiO_2 on the glass fibre membrane has been synthesized for photocatalytic OCM reaction.

https://doi.org/10.1038/s41560-023-01317-5

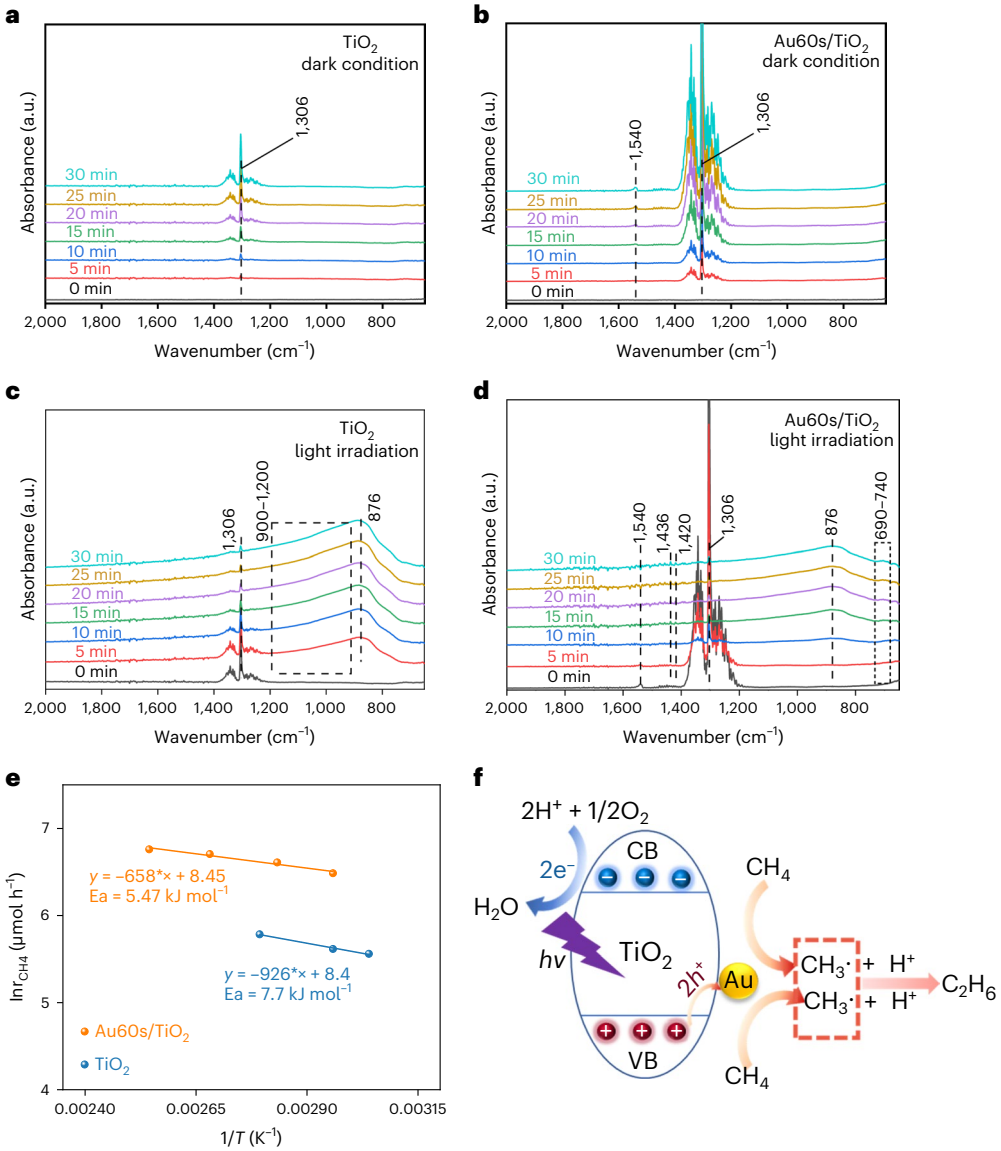

Fig. 4 | The interface reaction chemistry. a, In situ CH_4 adsorption ATR–FTIR spectrum for TiO_2 under dark condition. **b**, In situ CH_4 adsorption ATR–FTIR spectrum for Au60s/TiO_2 under dark condition. **c**, In situ ATR–FTIR spectra of photocatalytic methane conversion over TiO_2. **d**. In situ ATR–FTIR spectra of photocatalytic methane conversion over Au60s/TiO_2. Note: due to the weak adsorption of methane on ZeSe crystal detection window, the signal of methane can be observed only after its adsorption on the surface of catalysts during the test period (Supplementary Fig. 30). **e**, Kinetics of methane conversion over Au60s/TiO_2 and TiO_2 catalysts. *, multiple sign; x, independent variable. **f**, Proposed photocatalytic OCM process over Au60s/TiO_2.

The optimized Au60s/TiO_2 achieves a stable methane conversion rate (ca. 1.1 mmol h^{-1}), an attractive C_2/C_{2+} selectivity (around 90%) and a high AQE of 10.3 ± 0.6 at 365 nm. This results in a C_{2+} yield rate of 505 ± 15 μmol h^{-1}, which is at the same magnitude of order as the benchmark thermal catalysts operated at the high temperature (>680 °C). The high performance is attributed to the multi-functions of Au, including an efficient hole acceptor, methane adsorption and activation site and C–C coupling centre. Overall, the rapid fabrication process, high performance and in-depth understanding in this work represent a crucial progress in photocatalytic oxidation.

Methods

Materials preparation

A facile and rapid sputtering method was used to introduce metallic Au nanoparticles to TiO_2 layer on the support of a glass fibre membrane. Typically, certain amount of TiO_2 (anatase, Millennium PC-50) was dispersed in 500 ml of de-ionized water and the mixture was sonicated for 20 min to achieve a homogeneous suspension. Then, the mixture was filtered using a membrane (Ultrafine Glass Fibre Microporous Membrane, diameter 37 mm, pore size 0.22 μm, Shanghai Xingya Purification Material Factory) to form a uniform TiO_2 nanoparticle layer. The membrane was dried at 60 °C in the oven. The loading process of Au was carried out with a sputter machine (Agar Sputter Coater). The membrane loaded with TiO_2 was put on the middle of the round plate in the chamber. Next, the chamber was sealed, and a vacuum pump was turned on to evacuate the air. Then, certain amount of argon was introduced to the chamber and the sputter process was conducted using a current at ca. 30 mA. Different sputtering times could be set, and the optimized sample was obtained within 1 min. After refilling with air, the window of chamber was opened and the Au/TiO_2 sample on the glass fibre membrane was ready to use for photocatalytic OCM reaction. The Au/TiO_2 with different sputtering times were denoted as Au_x/TiO_2, x = 5, 10, 20, 40, 60, 90, 120, 240 s. While the Au/TiO_2 with different loading amount of TiO_2 were denoted as Au/TiO_2-y, y = 5, 10,

15, 20, 25, 30 mg. For the characterization requires powder form of sample for analysis, the optimized Au60s/TiO_2 was scratched from the glass fibre membrane.

Photocatalytic OCM reaction

The photocatalytic OCM experiments was conducted using a flow reactor with a temperature controller, as shown in Supplementary Fig. 4. Typically, the glass fibre membrane with Au/TiO_2 sample on top was transferred to the middle of the reactor. Then, a stainless ring was installed to fix the membrane. Next, a rubber O-ring and a stainless cap were used to seal the reactor. The membrane was irradiated by a 365 nm light-emitting diode (LED) (100 W) from the quartz window of the cap. The temperature of the catalyst bed could be monitored and controlled by the temperature probe with a thermocouple at the bottom. Three gases, simulated air (BOC, 99.999%), methane (BOC, 99.999%) and argon (BOC, 99.999%), were supplied to the reactor at different ratios controlled by three mass flow controllers (Bronkhorst). The reaction system was purged by the gas mixture with the setting ratio for at least 1 h to reach equilibrium before photocatalytic activity evaluation. The reactor was connected to two gas chromatographs (GCs) for product analysis. In the Agilent 7820 GC, a CarbonPlot column and a 5A molecular sieve were connected to the thermal conductivity detectors for the analysis of H_2, O_2, N_2 and CH_4. In addition, an HP-PLOT Q column connected to the flame ionization detectors (FID) was used to detect organic products, such as C_2H_4, C_2H_6, C_3H_6, C_3H_8, C_4H_8, C_4H_{10} and so on. Another Varian 450 GC equipped with a methanizer and an FID was used to accurately quantify the concentration of CO_2 or CO (the concentration of CO_2 and CO is often too low to be detected by the insensitive thermal conductivity detectors; an FID with a methanizer is highly recommended to make a reliable quantification and avoid over-estimation of the selectivity to target products). For the isotope labelling ^{13}C experiment, $^{13}CH_4$ was used as the reactant and the product was analysed by a GC–mass spectrometry instrument (GC 8890-MS 5977).

Materials characterizations

The powder XRD spectra were recorded with a Stoe STADI-P instrument (2° to 40°, step 0.5° at 5.0 s per step) using Mo Kα1 (wavelength 0.70930 Å, 50 kV and 30 mA), in which the Au/TiO_2 membranes were cut into small pieces to fit the disk sample holder. UV–Vis diffuse reflectance spectroscopy measurements were conducted by a SHIMADZU UV-2550 in reflectance mode using standard $BaSO_4$ powder as a reference. The relative reflectance was converted to the Kubelka–Munk function F(R) to study the optical properties. XPS analysis was carried out using a Thermoscientific XPS K-alpha, and the data were analysed with CasaXPS software using C 1 s peak at 284.8 eV for calibration. In situ XPS experiment was conducted using a Thermo Fisher ESCALAB 250Xi equipped with a 365 LED light source. SEM imaging was conducted using a Jeol JSM 7600 FEG-SEM with EDX module. STEM images were performed using a Cs-Corrected Jeol 2100FC Microscopy operating at 200 kV.

TAS

The fs–ns timescale transient absorption spectra were collected on a Harpia-TA spectrometer (Light Conversion). The pump light was generated using a Pharos-SP-10W (light conversion, full width at half maximum ~140 fs, 10 kHz, 1,030 nm) coupled to an optical parametric amplifier (Orpheus) for general of either 355 or 532 nm pump light with a power of 750 μW (5 kHz). A white light probe beam was generated by focusing 1,030 nm output onto a sapphire crystal within the Harpia spectrometer. The pump beam (ca. 0.6 mm diameter) and the probe beam (ca. 0.4 mm diameter) were overlapped on the sample position. Data were analysed using Carpetview software (Light Conversion).

The μs–s timescale TAS measurements were carried out using either the second (532 nm) or third harmonic (355 nm) output of a Nd:YAG laser (Continuum, Surelite I-10, 532 nm, 6 ns pulse width) and excitation (0.40 mJ cm^{-2} at 0.66 Hz). The laser output was transmitted to the sample via a liquid light guide. A 100 W tungsten lamp coupled with a monochromator (OBB Corp., typically set to 4 nm resolution) was used as the probe light. The change of optical density (ΔOD) of the sample was calculated through measuring the transmitted light using a Si Photodiode and a homemade amplification system coupled to both an oscilloscope (Textronix TDS 220) and data acquisition card (DAQ card, National Instruments NI-6221). The oscilloscope data were for the study at the microseconds timescale while the DAQ card covered milliseconds to seconds. The data were averaged over 200 laser shots per wavelength to improve the ratio of the signal to noise.

To synthesize the TiO_2 and Au/TiO_2 glass slides for TAS measurements, a doctor-bladed method was used to prepare homogeneous and transparent films on the glass slides. A commercial Titania paste (Aldrich) was selected as the precursor of TiO_2 and a thin layer of TiO_2 was deposited on a 2 × 2 cm^2 glass slide. Then, the glass slide was transferred to the Muffle furnace and heated at 490 °C for 2 h with a heating rate of 20 °C min^{-1}. After cooling to room temperature, a TiO_2-coated glass slide for TAS measurement was obtained. The loading of Au on this TiO_2 glass slide was via a simple photodeposition method. Typically, the TiO_2 glass slide was immersed in 10 ml of MeOH/H_2O solution (V_{H2O}:V_{MeOH} = 4:1) with a Au concentration of 0.1 mg ml^{-1}. After purging with argon for 3 min, the mixture was irradiated with a 365 nm LED light source (95 W) for 15 s, during which the argon gas was supplied constantly. Then, the Au/TiO_2 glass slide was rinsed with de-ionized water and dried at room temperature. Finally, the Au/TiO_2 glass slide was calcinated at 400 °C for 2 h with a heating rate of 20 °C min^{-1}. To make sure that the Au/TiO_2 on the glass slide is same as Au60s/TiO_2 prepared by the sputtering method, 22 Au/TiO_2 glass slides were fabricated, and the samples were scratched from each slide. The obtained powders were filtered on the glass fibre membrane and tested the photocatalytic OCM activity, which shows a similar activity (both C_2 yield rate and selectivity) to that of Au60s/TiO_2 (Supplementary Fig. 18). Thus, the Au/TiO_2 glass slide was used to carry out the TAS to explore the reaction mechanism on Au60s/TiO_2.

In situ EPR spectroscopy

In situ EPR was measured using a Bruker EMX PLUS spectrometer with a xenon lamp (300 W). During the experiments, the mixtures of 30 μl DMPO (200 mM in water) and 30 μl sample (1 mg ml^{-1} in water) were used for the detection of hydroxyl radicals. For the detection of superoxide radicals, 1 ml MeOH was added in the above mixture as the holes scavenger. The signals were recorded under dark condition and 5 min light irradiation, respectively.

In situ ATR–FTIR

The ATR–FTIR experiments were conducted using a Thermo Fisher Nicolet IS50 II FTIR spectrometer equipped with a liquid-nitrogen-cooled mercury-cadmium-telluride (MCT) detector. An internal reflection element made of ZnSe crystal integrated with a photocatalytic in situ photochemical IR accessory was obtained from LingLu Instrument. One milligram powder catalyst sample was spread on the surface of internal reflection element. A 45° ZnSe face-angled crystal was used as reflection element and the angle of incidence was set as ca. 70°.The absorbance spectra ranged from 4,000 to 650 cm^{-1} and was recorded by averaging 64 scans at a resolution of 2 cm^{-1}. The system was degassed for 0.5 h under Ar atmosphere to remove the absorbates. Each spectrum was recorded by averaging 64 scans at a resolution of 2 cm^{-1} and the final spectrum was obtained by subtraction of background. Before CH_4 introduction, the samples were measured again to obtain the 0 min spectrum. Subsequently, 50 ml min^{-1} CH_4 gas (99.999%) was introduced to the chamber and the spectrum was collected under the CH_4 atmosphere at 5, 10, 15, 20, 25 and 30 min. After 30 min of CH_4 adsorption process, the sample was irradiated by a 300 W xenon lamp (PLS-SXE300, Perfectlight) with a 380 nm filter. The spectrum was collected at 5, 10, 15, 20, 25 and 30 min.

The calculation of C_2/C_{2+} selectivity

The C_2/C_{2+} selectivity calculation was based on the observable products (C_2H_6, C_2H_4, C_3H_6, C_3H_8, C_4H_8, C_4H_{10} and CO_2) analysed, and the formula is shown below:

$$Sel_{C2} = \frac{2\times(n_{C2H6}+n_{C2H4})}{2\times n_{C2H6}+2\times n_{C2H4}+3\times n_{C3H8}+3\times n_{C3H6}+4\times n_{C4H8}+4\times n_{C4H10}+n_{CO2}}\times 100\%$$

$$Sel_{C2+} = \frac{2\times(n_{C2H6}+n_{C2H4})+3\times(n_{C3H8}+n_{C3H6})+4\times(n_{C4H10}+n_{C4H8})}{2\times n_{C2H6}+2\times n_{C2H4}+3\times n_{C3H8}+3\times n_{C3H6}+4\times n_{C4H8}+4\times n_{C4H10}+n_{CO2}}\times 100\%$$

where n is the yield rate of different products.

AQE

For the measurement of AQE, the light intensity of 365 nm LED was set to be 18.5 mW cm^{-2} to ensure the sufficient utilization of the photons by the photocatalyst. The reaction condition was the GHSV of 996,000 ml g_{cat}^{-1} h^{-1} with a ratio of CH_4 to O_2 at 133:1 operated at 120 °C. To confirm the reproducibility, four membranes prepared at different times were used for this measurement, and the average value was obtained. The calculation formula is shown below:

$$AQE = \frac{(2\times n_{C2H6}+4\times n_{C2H4}+4\times n_{C3H8}+6\times n_{C3H6}+6\times n_{C4H10}+8\times n_{C4H10}+8\times n_{CO2})\times N_A}{P\times A\times\frac{\lambda}{hc}\times t}\times 100\%$$

where n is the yield rate of different products, N_A is the Avogadro constant, P is the light intensity (18.5 mW cm^{-2}), A is the irradiation area (ca. 7 cm^2), λ is the wavelength of the irradiation light (365 nm), h is the Planck's constant, c is the speed of light and t is the time.

Data availability

The authors declare that all data supporting the findings of this study are available within the paper, supplementary information files and the provided source data files. Source data are provided with this paper.

References

1. Li, X., Wang, C. & Tang, J. Methane transformation by photocatalysis. *Nat. Rev. Mater.* **7**, 617–632 (2022).
2. Li, X., Pei, C. & Gong, J. Shale gas revolution: catalytic conversion of C1–C3 light alkanes to value-added chemicals. *Chem* **7**, 1755–1801 (2021).
3. Wang, Y., Hu, P., Yang, J., Zhu, Y. & Chen, D. C–H bond activation in light alkanes: a theoretical perspective. *Chem. Soc. Rev.* **50**, 4299–4358 (2021).
4. Farrell, B. L., Igenegbai, V. O. & Linic, S. A viewpoint on direct methane conversion to ethane and ethylene using oxidative coupling on solid catalysts. *ACS Catal.* **6**, 4340–4346 (2016).
5. Si, J. et al. Oxidative coupling of methane: examining the inactivity of the MnO_x–Na_2WO_4/SiO_2 catalyst at low temperature. *Angew. Chem. Int. Ed.* **61**, e202117201 (2022).
6. Arndt, S. et al. A critical assessment of Li/MgO-based catalysts for the oxidative coupling of methane. *Catal. Rev. Sci. Eng.* **53**, 424–514 (2011).
7. Kuo, J. C. W., Kresge, C. T. & Palermo, R. E. Evaluation of direct methane conversion to higher hydrocarbons and oxygenates. *Catal. Today* **4**, 463–470 (1989).
8. Singh, S. P., Anzai, A., Kawaharasaki, S., Yamamoto, A. & Yoshida, H. Non-oxidative coupling of methane over Pd-loaded gallium oxide photocatalysts in a flow reactor. *Catal. Today* **375**, 264–272 (2021).
9. Li, X., Xie, J., Rao, H., Wang, C. & Tang, J. Platinum- and CuO_x-decorated TiO_2 photocatalyst for oxidative coupling of methane to C_2 hydrocarbons in a flow reactor. *Angew. Chem. Int. Ed.* **59**, 19702–19707 (2020).
10. Singh, S. P. et al. A Pd-Bi Dual-Cocatalyst-Loaded Gallium oxide photocatalyst for selective and stable nonoxidative coupling of methane. *ACS Catal.* **11**, 13768–13781 (2021).
11. Song, S. et al. A selective Au–ZnO/TiO_2 hybrid photocatalyst for oxidative coupling of methane to ethane with dioxygen. *Nat. Catal.* **4**, 1032–1042 (2021).
12. Souza, J. D., Souza, V. S. & Scholten, J. D. Synthesis of hybrid zinc-based materials from ionic liquids: a novel route to prepare active zn catalysts for the photoactivation of water and methane. *ACS Sustain. Chem. Eng.* **7**, 8090–8098 (2019).
13. Meng, L. et al. Gold plasmon-induced photocatalytic dehydrogenative coupling of methane to ethane on polar oxide surfaces. *Energy Environ. Sci.* **11**, 294–298 (2018).
14. Wu, X. Y. et al. Visible-light driven room-temperature coupling of methane to ethane by atomically dispersed Au on WO3. *J. Energy Chem.* **61**, 195–202 (2021).
15. Huang, H. et al. Site-sensitive selective CO_2 photoreduction to CO over gold nanoparticles. *Angew. Chem. Int. Ed.* **61**, 1–7 (2022).
16. Kumar, A. A review on the factors affecting the photocatalytic degradation of hazardous materials. *Mater. Sci. Eng. Int. J.* **1**, 106–114 (2017).
17. Meng, F. et al. Temperature dependent photocatalysis of g-C_3N_4, TiO_2 and ZnO: differences in photoactive mechanism. *J. Colloid Interface Sci.* **532**, 321–330 (2018).
18. Young, A. J. et al. One-step synthesis and XPS investigations of chiral NHC-Au(0)/Au(i) nanoparticles. *Nanoscale* **11**, 8327–8333 (2019).
19. Klyushin, A. Y., Rocha, T. C. R., Hävecker, M., Knop-Gericke, A. & Schlögl, R. A near ambient pressure XPS study of Au oxidation. *Phys. Chem. Chem. Phys.* **16**, 7881–7886 (2014).
20. Tang, J., Durrant, J. R. & Klug, D. R. Mechanism of photocatalytic water splitting in TiO_2. Reaction of water with photoholes, importance of charge carrier dynamics, and evidence for four-hole chemistry. *J. Am. Chem. Soc.* **130**, 13885–13891 (2008).
21. Yamada, M. & Nishihara, H. Large solvent and potential effects on the collective surface plasmon band of gold nanoparticle films. *ChemPhysChem* **5**, 555–559 (2004).
22. Chapman, R. & Mulvaney, P. Electro-optical shifts in silver nanoparticle films. *Chem. Phys. Lett.* **349**, 358–362 (2001).
23. Kedawat, G. et al. Studies of ultrafast transient absorption spectroscopy of gold nanorods in an aqueous solution. *ACS Omega* **4**, 12626–12631 (2019).
24. Li, X., Yu, J. & Jaroniec, M. Hierarchical photocatalysts. *Chem. Soc. Rev.* **45**, 2603–2636 (2016).
25. Yu, X. et al. Stoichiometric methane conversion to ethane using photochemical looping at ambient temperature. *Nat. Energy* **5**, 511–519 (2020).
26. Chen, X. et al. Photocatalytic oxidation of methane over silver decorated zinc oxide nanocatalysts. *Nat. Commun.* **7**, 12273 (2016).
27. Jiang, W. et al. Pd-modified ZnO–Au enabling alkoxy intermediates formation and dehydrogenation for photocatalytic conversion of methane to ethylene. *J. Am. Chem. Soc.* **143**, 269–278 (2021).
28. Zhang, W. et al. High-performance photocatalytic nonoxidative conversion of methane to ethane and hydrogen by heteroatoms-engineered TiO_2. *Nat. Commun.* **13**, 2806 (2022).
29. Finnie, K. S., Luca, V., Moran, P. D., Bartlett, J. R. & Woolfrey, J. L. Vibrational spectroscopy and EXAFS study of Ti(OC_2H_5)$_4$ and alcohol exchange in Ti(iso-OC_3H_7)$_4$. *J. Mater. Chem.* **10**, 409–418 (2000).

30. Tao, F. F. et al. Understanding complete oxidation of methane on spinel oxides at a molecular level. *Nat. Commun.* **6**, 7798 (2015).
31. Lang, J., Ma, Y., Wu, X., Jiang, Y. & Hu, Y. H. Highly efficient light-driven methane coupling under ambient conditions based on an integrated design of a photocatalytic system. *Green Chem.* **22**, 4669–4675 (2020).
32. Mowbray, D. J., Migani, A., Walther, G., Cardamone, D. M. & Rubio, A. Gold and methane: a noble combination for delicate oxidation. *J. Phys. Chem. Lett.* **4**, 3006–3012 (2013).
33. Singh, S. P., Yamamoto, A. & Yoshida, H. Nonoxidative coupling of ethane with gold loaded photocatalysts. *Catal. Sci. Technol.* **12**, 1551–1561 (2022).
34. Wu, S. et al. Ga-doped and Pt-loaded porous TiO_2–SiO_2 for photocatalytic nonoxidative coupling of methane. *J. Am. Chem. Soc.* **141**, 6592–6600 (2019).
35. Li, L. et al. Efficient sunlight-driven dehydrogenative coupling of methane to ethane over a Zn^+-modified zeolite. *Angew. Chem. Int. Ed.* **50**, 8299–8303 (2011).
36. Amano, F. & Ishimaru, M. Hydroxyl radical formation on metal-loaded Ga_2O_3 photocatalysts for dehydrogenative coupling of methane to ethane with water. *Energy Fuels* **36**, 5393–5402 (2022).
37. Ishimaru, M., Amano, F., Akamoto, C. & Yamazoe, S. Methane coupling and hydrogen evolution induced by palladium-loaded gallium oxide photocatalysts in the presence of water vapor. *J. Catal.* **397**, 192–200 (2021).

Acknowledgements

X.L., Y.X. and J.T. are grateful to the UK EPSRC (EP/S018204/2). J.T. thanks the Tsinghua University Initiative Scientific Research Program for support. X.L. and J.T. also acknowledge the European Union's Horizon Europe research and innovation programme under grant agreement no. 101070721 (project acronym 'GH2'). X.L. acknowledges a UCL PhD studentship (GRS and ORS). We all are grateful to J. Yu and Y. Yang for in situ XPS characterization. The STEM observations were performed at the Albert Crewe Centre for electron microscopy, a University of Liverpool shared research facility that is free at the point of use for all academic users. We are also grateful to Z. Zeng for help with picture embellishment.

Author contributions

J.T. designed the project and supervised the progress of the whole project. X.L. proposed the idea, designed and conducted experiments, analysed data and drafted the article. Y.X. assisted with activity test and contributed to the discussion of the photocatalytic mechanism. C.L. and A.J.C. conducted the TAS measurement. Q.L. carried out in situ ATR–FTIR measurements. M.B. and N.D.B. carried out the STEM. L.Z. assisted with the Au sputter process.

Competing interests

The authors declare no competing interests.

Additional information

Supplementary information The online version contains supplementary material available at https://doi.org/10.1038/s41560-023-01317-5.

Correspondence and requests for materials should be addressed to Alexander J. Cowan or Junwang Tang.

Peer review information *Nature Energy* thanks Jinlin Long, Hisao Yoshida and the other, anonymous, reviewer(s) for their contribution to the peer review of this work.